Resistance to PARP inhibition by DNA damage response alterations in BRCA1/2-deficient tumors

Gogola, E.

Citation

Gogola, E. (2019, November 12). *Resistance to PARP inhibition by DNA damage response alterations in BRCA1/2-deficient tumors*. Retrieved from https://hdl.handle.net/1887/80398

Author: Gogola, E.
Title: Resistance to PARP inhibition by DNA damage response alterations in BRCA1/2-deficient tumors
Issue Date: 2019-11-12

CHAPTER 5

Homologous recombination is frequently restored in BRCA1- but not BRCA2-deficient tumors that acquired PARP inhibitor resistance

Ewa Gogola, Frank Rolfs*, Jinhuyk Bhin*, Sander R. Piersma,
Roebi de Bruijn, Julian R. de Ruiter, Bram van den Broek, Mariana P. Dias,
Alexandra A. Duarte, Wendy Sol, Marieke van de Ven, Lodewyk F. A. Wessels,
Connie R. Jimenez, Piet Borst, Sven Rottenberg and Jos Jonkers

*equal contribution

In preparation

ABSTRACT

BRCA1 and BRCA2 are two tumor suppressors that operate on a common pathway to repair DNA double-strand breaks by homologous recombination (HR); thereby maintaining genome stability and cellular viability. Loss-of-function of either of these proteins is frequently found in breast and ovarian cancer patients and also occurs in other tumors, including prostate, gastric and pancreatic cancer. Due to the HR defect BRCA1/2-deficient cancers are sensitive to poly(ADP-ribose) polymerase inhibitors (PARPi). Despite the epistatic relationship of BRCA1 and BRCA2, the fact that PARPi sensitivity can be rescued by the loss of the 53BP1/RIF1/REV7 pathway in BRCA1- but not in BRCA2-deficient cells provides an intriguing distinction between these well-known DNA repair factors. Here we analyzed 47 BRCA1/p53- and 26 BRCA2/p53-deficient PARPi-resistant mouse mammary tumors for their capacity to restore ionizing radiation-induced RAD51 foci as functional surrogate of HR activity. Whereas all therapy-naïve tumors remained incapable of forming RAD51 foci, nearly 2/3 of the PARPi-resistant BRCA1/p53-deficient tumors restored RAD51 foci formation. Since the restoration was only partial and never to the level of the p53-deficient control, our data show that loss of BRCA1 function cannot easily be rescued in a complete fashion. As underlying mechanism of the secondary resistance, our multi-omics analysis revealed the loss of *Shld2* in addition to *Trp53bp1*, *Rif1*, or *Rev7* depletion. In clear contrast, the loss of BRCA2 could not be compensated in any of the PARPi-resistant tumors, as judged from the regain of RAD51 foci. Our results suggest that, in addition to their epistatic relationship, BRCA2 is indispensable for homology-directed DNA repair in mice, whereas BRCA1 function can be partially restored to a level sufficient to cause PARPi resistance.

INTRODUCTION

The observation that many oncogenic events render cancer cells reliant on specific and druggable biological pathways is a premise of targeted therapies for personalized cancer treatment. Unfortunately, the selective pressure that initially kills cancer cells is also a driving force in selecting cells which acquired drug resistance. A better understanding of the recurrent molecular patterns of resistance in specific genetic contexts is therefore instrumental to improve clinical outcomes[1,2]. Moreover, modelling drug resistance is also a great tool to understand complex relationships between genes involved in fundamental cellular processes.

Dysfunctional repair of DNA double strand breaks (DSBs) by homologous recombination (HR) represents one of the cancer deficiencies that can be exploited therapeutically. This can be achieved by the inhibition of poly(ADP-ribose) polymerase (PARP) enzymes PARP1 and PARP2[3,4]. PARP1/2 have been implicated in several DNA damage response (DDR) pathways, including the repair of DNA single strand breaks (SSBs), DSBs and stabilization of replication forks (RFs)[5]. Catalytic inhibition as well as trapping of PARP1/2 on the DNA by clinical PARP inhibitors (PARPi) leads to replication-coupled DSBs formation, which in turn requires HR for efficient repair[6–9].

Although inactivating mutations of the core HR genes are frequently found across different tumor types[10–13], germline or somatic mutations in *BRCA1* and *BRCA2* genes remain the main biomarker of PARPi sensitivity in the clinical setting[14]. Currently, four different PARPi have been granted regulatory approval to treat BRCA-associated breast and ovarian cancers. Despite the clinical benefit, sustained antitumor responses to PARPi are often hampered by the emergence of resistance[15].

Previous studies have delineated several mechanisms by which BRCA-deficient tumors evade PARPi toxicity[8]. Independently of HR, PARPi resistance may be induced through (a) cellular extrusion of PARPi by upregulation of the drug efflux transporter P-gp[16]; (b) partial restoration of catalytic PARP activity through loss of poly(ADP-ribose) glycohydrolase (PARG)[17]; (c) inactivation of SLFN11[18,19] and (d) protection of stalled RFs[20]. All these mechanisms result in PARPi resistance by limiting PARPi-induced DNA damage, rather than restoring the capacity of BRCA-deficient cells to efficiently repair DSBs. In contrast, secondary (epi)genetic events that lead to reactivation of functional BRCA may fully cancel the initial susceptibility to PARPi due to HR restoration. Revertant mutations of *BRCA* genes have been found in a substantial proportion, but not in all patients with refractory tumors[21,22], suggesting that BRCA-independent PARPi resistance is relevant in the clinic. Moreover, genetic screens and *in vivo* studies in preclinical models demonstrated that BRCA1 is dispensable for the HR recovery, at least partially. Inactivation of the 53BP1-RIF1-shieldin pathway, which inhibits HR and is antagonized by BRCA1 during S phase, was shown to partially restore HR and to confer PARPi resistance in BRCA1-deficient cells[8]. Consistent with different roles of BRCA1 and BRCA2 in HR, abrogation of the 53BP1-RIF1-shieldin pathway failed to restore HR in the absence of BRCA2, suggesting context specificity of HR recovery. This poses the question whether BRCA2 is essential for the HR, which would have important implications for PARPi resistance. It is also not clear what the contributions of HR-dependent and -independent PARPi resistance mechanisms are in tumors that cannot restore functional BRCA1/2. Here, we address these questions using a unique collection of matched PARPi-naïve and -resistant tumors derived from genetically engineered mouse models (GEMMs) of BRCA1/2-associated cancer.

RESULTS

An *in situ* RAD51 IRIF assay reveals context specificity of PARPi-induced HR recovery

To study the contribution of different PARPi resistance mechanisms *in vivo*, we assessed the HR status of a cohort of matched PARPi-naïve and -resistant mouse mammary tumors that we derived from our *Kcre14; Trp53*$^{F/F}$*; Brca1*$^{F/F}$ (KB1P), *K14cre; Trp53*$^{F/F}$*; Brca1*$^{F/F}$*; Mdr1a/b*$^{-/-}$ (KB1PM) and *Kcre14; Trp53*$^{F/F}$*; Brca2*$^{F/F}$ (KB2P) GEMM mice[16,17,23–25]. We have shown previously that PARPi resistance can be induced in these models by long-term treatment with PARPi and it is preserved upon tumor passaging[23,26]. Moreover, it is impossible that the acquired resistance in our models is BRCA-related, as these tumors harbor large intragenic deletions in the *Brca1* or *Brca2* genes[24,25]. Although we have demonstrated that upregulation of the P-gp transporter is a frequent event in mouse tumors exposed to PARPi[16], the evidence of its involvement in the clinical setting is still lacking. We have therefore excluded the possibility of P-gp-mediated resistance to PARPi olaparib by either genetic depletion of P-gp (encoded by *Mdr1a/b* genes; KB1PM model) or by using the PARPi AZD2461 which is a poor substrate for this transporter (KB1P and KB2P models)[23,27].

First, we established a functional HR assay using RAD51 ionizing radiation-induced foci (RAD51 IRIF) as a surrogate of HR activity. RAD51 recombinase facilitates homologous pairing and strand invasion, which is central to homology-directed repair[28]. Briefly, cryopreserved PARPi-naïve and -resistant tumors were orthotopically transplanted into syngeneic recipient mice, and upon outgrowth to 500 mm^3 DNA damage was inflicted by locally applied ionizing radiation (IR) at the dosage of 15 Gy. 2 hr post-irradiation, tumors were isolated and formalin-fixed paraffin-embedded (FFPE) tissues were used for RAD51 immunofluorescence imaging, followed by unbiased automated foci quantification (**Fig. 1a**). Of note, all tumors exhibited high growth rates prior to the irradiation, suggesting low levels of cell cycle arrest that could influence the HR score (**Supplementary Fig. 1a, b**). Moreover, the data show no growth difference between PARPi-naïve and -resistant

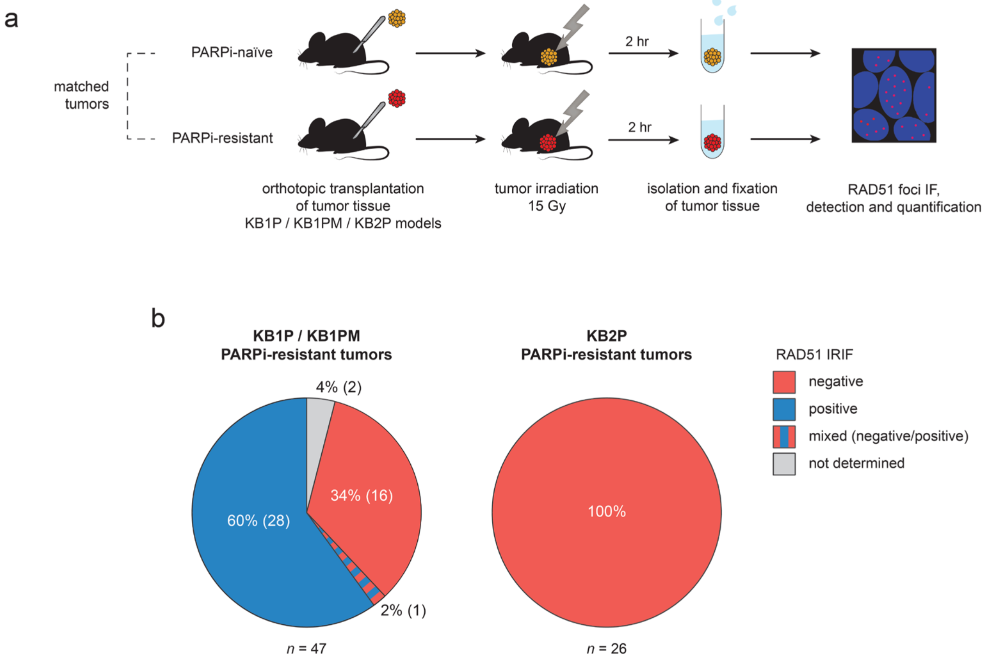

Figure 1. *In situ* RAD51 IRIF assay reveals context specificity of PARPi-induced HR recovery. **a**, Schematic representation of the RAD51 IRIF formation assay. **b**, Pie charts showing the outcome of the RAD51 IRIF assay in PARPi-resistant KB1P(M) and KB2P tumor cohorts; percentages and numbers of individual tumors analyzed are indicated; n – total number of individual tumors from the indicated models. See also Supplementary Fig. 1 and Supplementary Fig. 2.

tumors. As positive control for this assay we used an HR-proficient tumor derived from the *K14cre; Trp53*$^{F/F}$ (KP) model. Two different factors were tested to optimize the assay: IR dosage (15 and 24 Gy) and post-irradiation incubation time (1-6 hr). We did not observe significant differences in RAD51 IRIF formation between the two IR dosages, and the highest accumulation of RAD51 foci was detected 2 hours after induction of DNA damage (**Supplementary Fig. 1c-e**).

As expected, we did not detect any RAD51 IRIF formation in any of the PARPi-naïve tumors (**Supplementary Fig. 2a**), confirming that the *Brca1/2* mutations induced in our models completely abolish HR repair. This is consistent with the fact that all tumors initially responded to PARPi, as shown previously[17,29]. Nevertheless, the tumors eventually developed stable secondary resistance. Analysis of the 47 individual BRCA1-deficient PARPi-resistant tumors revealed that 62% (29/47) of the tumors have restored the capacity to form RAD51 foci, including one tumor with a mixed pattern (RAD51 IRIF positive and negative areas) (**Fig. 1b**). These results suggest that HR recovery is a predominant but not the only mechanism of PARPi resistance in the BRCA1 model. In contrast, none of the 26 PARPi-resistant BRCA2-deficient tumors exhibited the RAD51 IRIF-positive phenotype (**Fig. 1b**) (*P*=0.0001, two-tailed Fisher's exact test). Given that PARPi treatment is a potent trigger of HR restoration in the KB1P(M) models, the negative RAD51 score of the BRCA2-deficient cohort strongly indicates that BRCA2 is indispensable for competent HR.

The 53BP1 pathway is frequently inactivated in PARPi-resistant HR-proficient KB1P(M) tumors

Using whole-exome sequencing we excluded the possibility that our KB1P(M) or KB2P mouse mammary tumors still contain tumor cells with a *Brca1/2* wild-type allele selected during PARPi therapy (**Supplementary Fig. 2b**). We then determined the contribution of 53BP1 inactivation to the HR-related PARPi resistance in the KB1P(M) tumors. To this end, we combined the immunohistochemistry (IHC) analysis of the 53BP1 protein expression with the functional analysis of 53BP1 IRIF formation, using the same protocol as for the RAD51 IRIF. Both approaches yielded consistent results, identifying 13 individual PARPi-resistant KB1P(M) tumors with loss of the 53BP1 protein (**Fig. 2a-c**). All of the 53BP1-deficient samples were scored as RAD51 IRIF positive and no evidence of 53BP1 loss was found in PARPi-naïve or BRCA2-deficient tumors, consistent with the antagonistic relationship between 53BP1 and BRCA1 in the regulation of the DSB pathway choice (**Fig. 2a and Supplementary Fig. 2a**). Of note, 5 of the 13 53BP1-depleted tumors harbor previously identified inactivating mutations in *Trp53bp1* gene[23], and therefore served as internal positive controls in our assay (**Fig. 2a**). Moreover, among the 13 tumors 4 exhibited nests of 53BP1-positive or-negative tumor cells, strongly suggesting intratumoral heterogeneity of PARPi resistance mechanisms. The mixed RAD51 IRIF profile seen for one of these 4 tumors confirms this notion (**Fig. 2a**).

We have previously reported that HR-related resistance to PARPi in KB1P(M) tumors can also be triggered by the loss of the 53BP1 downstream effector protein REV7[30], which is part of the shieldin complex[31–34]. We therefore matched our existing REV7 protein expression data (ref[30]) with the RAD51/53BP1 results and found that REV7 depletion was mutually exclusive with the loss of 53BP1. In most cases (4/5) we found an association with restoration of RAD51 IRIF, and the one exception is most likely also due to intratumoral heterogeneity (**Fig. 2a** and **2b**). These results further corroborate the importance of the 53BP1-RIF1-shieldin pathway for the PARPi response in the BRCA1-deficient context.

High-throughput multi-omics analysis in the KB1P(M) model identifies potential factors of PARPi resistance

Post-translational modifications (PTMs), such as protein phosphorylation, are key to spatiotemporal and integrative regulation of the DDR. Thus, to explore potential alterations

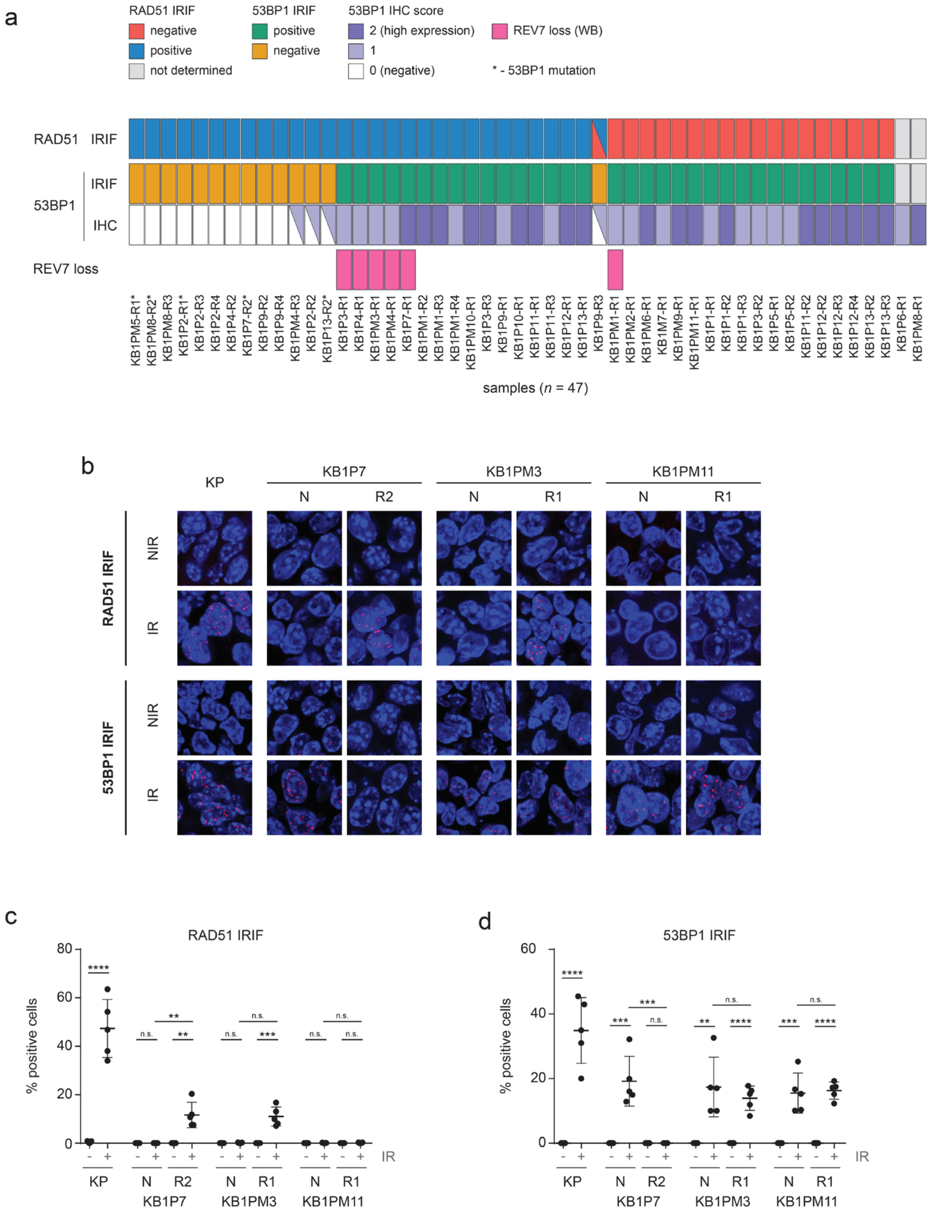

Figure 2. The 53BP1 pathway is frequently inactivated in HR-proficient PARPi-resistant tumors. **a**, Oncoplot showing the outcome of the indicated assays for the KB1P(M) PARPi-resistant tumors; N – naïve, R – resistant, WB – western blotting. Tumors harboring previously reported mutations in the *Trp53bp1* gene[23] are marked with asterisk. **b-d**, Representative images (b) and quantification (c-d) of the RAD51 and 53BP1 IRIFs for the three different matched KB1P(M) tumor pairs; IR – irradiated, NIR – non irradiated; scale bar, 100 µm; data in (c-d) represented as percentage of positive cells (>5 foci/nucleus) per imaged area (single data point, typically 100-200 cells/area); $****P < 0.0001$, $***P < 0.001$, $** P < 0.01$ (two-tailed Mann-Whitney U test). See also Supplementary Fig. 2.

in DDR signaling induced by PARPi resistance we used quantitative mass spectrometry to profile DDR-dependent phosphorylation in KB1P(M) tumors. For this purpose, we used snap-frozen tissue samples generated during the RAD51/53BP1 IRIF analyses, in which DNA damage was triggered by IR (15 Gy, 2 hr recovery). We focused on 12 matched (naïve/resistant) tumor pairs, selected based on their HR status (positive/negative) and plausible mechanism of resistance (53BP1 loss/REV7 loss/unknown) (**Fig. 3a**). We applied titanium dioxide (TiOx)-based method for the global phosphopeptide enrichment and single-shot liquid chromatography-tandem mass spectroscopy (LC-MS/MS) label-free phosphoproteomics for peptide detection and quantification. Moreover, flow-through fractions after TiOX enrichment were collected for the LC-MS/MS proteome analysis (**Fig. 3b**).

For proof-of-concept, we first carried out differential expression (DE) analyses on proteomics and phosphoproteomics datasets, between non-irradiated (NIR) and irradiated (IR) samples. As expected, irradiation had much more profound effect on global protein phosphorylation than on protein expression at 2 hr time-point (**Fig. 3c**). Moreover, gene ontology (GO) analysis revealed that DDR-related pathways were significantly enriched (top ranked) upon irradiation, and this pathway signature was very distinct from that of unchallenged tumors (**Fig. 3d** and **Supplementary Fig. 3a**). As shown in **Fig. 3e**, among substrates whose phosphorylation was induced by IR treatment were factors with known functions in DSB repair (including core HR factors as well as 53BP1 and its interactors, RIF1 and Paxip1), DNA damage checkpoint signaling/activation, DNA replication and histone modification. To further validate our dataset, we attempted to identify the putative protein kinases responsible for the differential phosphorylation of target proteins using NetworKIN[35], an integrative computational approach that combines consensus sequence motifs with protein association networks. Because current tools, including NetworKIN, can only predict cognate kinases using human datasets, we first mapped mouse phosphosites to their human orthologs using PhosphoSitePlus database[36]. Cross-species mapping has obvious limitations, as it restricts the experimental dataset to known orthologous phosphosites. Despite this, our analysis identified the Ser/Thr protein kinase ataxia-telangiectasia mutated (ATM) as a major upstream IR-regulatory kinase, consistent with previous reports[37–39] (**Supplementary Fig. 3b**). Also recovered by NetworKIN were Rad3-related (ATR) and DNA-dependent protein kinase (DNA-PK). ATR and DNA-PK are, next to ATM, two of the most prominent DDR kinases and their IR-induced activation through ATM-mediated phosphorylation is well documented[40]. Other kinases that were predicted to contribute to IR response in our models include catalytic subunit of casein kinase 2 (CK2alpha), which regulates early steps in DSB repair[40], and TTK (also known as Mps1), a mitotic kinase with attributed roles in the maintenance of the IR-induced G2/M checkpoint[41,42]. In parallel to the kinase prediction approach, we also performed an unbiased sequence motif analysis

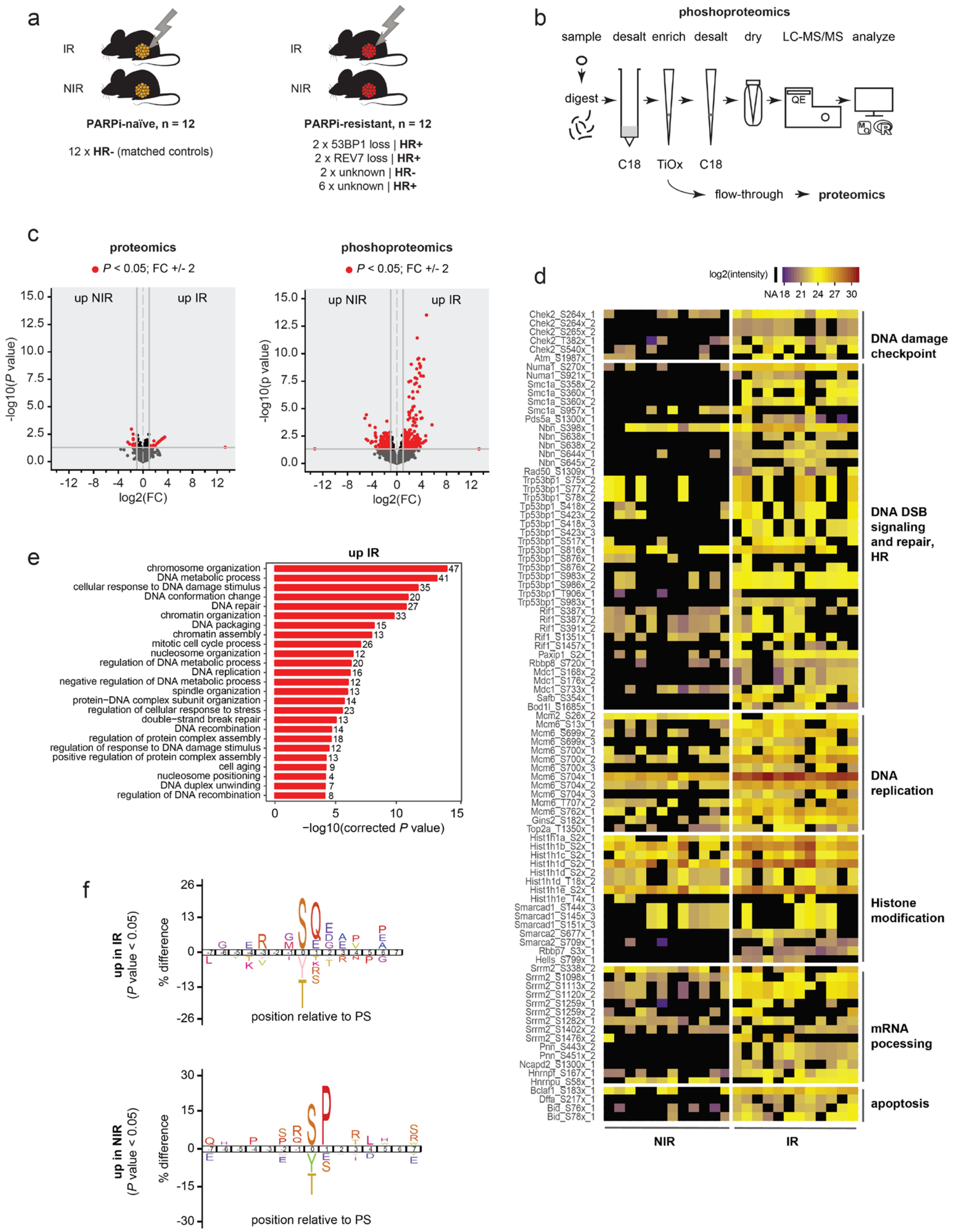
a
IR
NIR
PARPi-naïve, n = 12
12 x HR- (matched controls)
IR
NIR
PARPi-resistant, n = 12
2 x 53BP1 loss | HR+
2 x REV7 loss | HR+
2 x unknown | HR-
6 x unknown | HR+
b
phosphoproteomics
sample
desalt
enrich
desalt
dry
LC-MS/MS
analyze
digest
QE
C18
TiOx
C18
flow-through
proteomics
c
proteomics
P < 0.05; FC +/- 2
up NIR
up IR
-log10(P value)
log2(FC)
15.0
12.5
10.0
7.5
5.0
2.5
0.0
-12
-8
-4
0
4
8
12
phosphoproteomics
P < 0.05; FC +/- 2
up NIR
up IR
-log10(p value)
log2(FC)
d
log2(intensity)
NA 18 21 24 27 30
Chek2_S264x_1
Chek2_S264x_2
Chek2_S265x_2
Chek2_T382x_1
Chek2_S540x_1
Atm_S1987x_1
Numa1_S270x_1
Numa1_S921x_1
Smc1a_S358x_2
Smc1a_S360x_1
Smc1a_S360x_2
Smc1a_S957x_1
Pds5a_S1300x_1
Nbn_S398x_1
Nbn_S638x_1
Nbn_S638x_2
Nbn_S644x_1
Nbn_S645x_2
Rad50_S1309x_1
Trp53bp1_S75x_2
Trp53bp1_S77x_2
Trp53bp1_S78x_2
Tp53bp1_S418x_2
Tp53bp1_S423x_2
Tp53bp1_S418x_3
Tp53bp1_S423x_3
Trp53bp1_S517x_1
Trp53bp1_S816x_1
Trp53bp1_S876x_1
Trp53bp1_S876x_2
Trp53bp1_S983x_2
Trp53bp1_S986x_2
Trp53bp1_T906x_1
Trp53bp1_S983x_1
Rif1_S387x_1
Rif1_S387x_2
Rif1_S391x_2
Rif1_S1351x_1
Rif1_S1457x_1
Paxip1_S2x_1
Rbbp8_S720x_1
Mdc1_S168x_2
Mdc1_S176x_2
Mdc1_S733x_1
Safb_S354x_1
Bod1l_S1685x_1
Mcm2_S26x_2
Mcm6_S13x_1
Mcm6_S699x_2
Mcm6_S699x_3
Mcm6_S700x_1
Mcm6_S700x_2
Mcm6_S700x_3
Mcm6_S704x_1
Mcm6_S704x_2
Mcm6_S704x_3
Mcm6_T707x_2
Mcm6_S762x_1
Gins2_S182x_1
Top2a_T1350x_1
Hist1h1a_S2x_1
Hist1h1b_S2x_1
Hist1h1c_S2x_1
Hist1h1d_S2x_1
Hist1h1d_S2x_2
Hist1h1d_T18x_2
Hist1h1e_S2x_1
Hist1h1e_T4x_1
Smarcad1_S144x_3
Smarcad1_S145x_3
Smarcad1_S151x_3
Smarca2_S677x_1
Smarca2_S709x_1
Rbbp7_S3x_1
Hells_S799x_1
Srrm2_S338x_2
Srrm2_S1098x_1
Srrm2_S1113x_2
Srrm2_S1120x_2
Srrm2_S1259x_1
Srrm2_S1259x_2
Srrm2_S1282x_1
Srrm2_S1402x_2
Srrm2_S1476x_2
Pnn_S443x_2
Pnn_S451x_2
Ncapd2_S1300x_1
Hnrnpf_S167x_1
Hnrnpu_S58x_1
Bclaf1_S183x_1
Dffa_S217x_1
Bid_S76x_1
Bid_S78x_1
DNA damage checkpoint
DNA DSB signaling and repair, HR
DNA replication
Histone modification
mRNA pocessing
apoptosis
NIR
IR
e
up IR
chromosome organization 47
DNA metabolic process 41
cellular response to DNA damage stimulus 35
DNA conformation change 20
DNA repair 27
chromatin organization 33
DNA packaging 15
chromatin assembly 13
mitotic cell cycle process 26
nucleosome organization 12
regulation of DNA metabolic process 20
DNA replication 16
negative regulation of DNA metabolic process 12
spindle organization 13
protein−DNA complex subunit organization 14
regulation of cellular response to stress 23
double−strand break repair 13
DNA recombination 14
regulation of protein complex assembly 18
regulation of response to DNA damage stimulus 12
positive regulation of protein complex assembly 13
cell aging 9
nucleosome positioning 4
DNA duplex unwinding 7
regulation of DNA recombination 8
0
5
10
15
−log10(corrected P value)
f
up in IR
(P value < 0.05)
% difference
26
13
0
-13
-26
position relative to PS
up in NIR
(P value < 0.05)
% difference
30
15
0
-15
-30
position relative to PS

to identify consensus amino acid patterns of phosphorylation events. As shown in **Fig. 3f**, the IR signature was dominated by the serine or threonine residues followed by glutamine (SQ/TQ) motifs, which are known to be preferentially phosphorylated by ATM and ATR in response to DNA damage. Altogether, these results validate this approach in detecting DNA-damage dependent protein phosphorylation events in irradiated tumor samples.

To identify alterations specifically induced by PARPi treatment, we then integrated the generated phosphoproteomic and proteomic information with genomic and transcriptomic deep-sequencing data for a comparative multi-omics analysis of naïve versus resistant tumors (**Fig. 4a**). To this end, we performed RNA (RNA-seq), whole-exome (Exome-Seq) and copy-number variation (CNV-Seq) sequencing of the KB1P(M) tumors (21 naïve and 44 resistant tumors, derived from 21 individual spontaneous tumors). We carried out a series of enrichment analyses to select differentially expressed genes, proteins and phosphosites (DEGs, DEPs and DPPs, respectively), CNV-seq analysis to identify acquired copy number events (focal gain/losses) and RNA-Seq-based analysis for the detection of gene fusions. Indels and single nucleotide variants (SNVs) were called using both Exome-Seq and RNA-Seq data. Through these efforts, we have obtained an initial set of 3727 candidates (**Fig. 4b** and **Supplementary Table 1**). Obviously, the majority of these alterations accrued stochastically as passenger rather than actionable aberrations that confer PARPi resistance. Thus, to enrich for plausible driver events, we prioritized candidates that: (1) were identified independently by at least two analyses ('multi-hits') or (2) have been implicated in the DDR ('DDR', based on PubMed search[17]) (**Figure 4a, b**). Importantly, frequency analyses integrating data across different omic platforms ('multi-hits') will fail to identify events restricted to one biochemical domain (e.g. mutation or phosphorylation), but nonetheless important for the biological process. As shown by previous studies, such discrete alterations may instead impact the expression of interacting partners or factors that share the same biological pathway[43]. To correct for this in the prioritization process, we applied a network-based algorithm DriverNet which relates aberrations to a disrupted patterns between two datasets based on known gene/protein associations[43]. Overall, the prioritization process yielded a final list of 891 putative PARPi

---

◀ **Figure 3** Ionizing radiation-induced phosphorylation in KB1P(M) tumors. **a**, Overview of the samples used in this study. **b**, A workflow of the global phosphoproteomics; C18 – desalting column/tip, TiOx – titanium dioxide. **c**, Volcano plots showing differentially expressed proteins (left panel) and phopshosites (right panel) between NIR and IR tumors; cutoffs for p value and fold change are marked with grey continuous lines (*P* = 0.05, FC = -/+ 2; limma); significant events with -2 > FC > 2 are shown in red, significant events that did not pass FC cutoff are shown in black and events with *P* > 0.05 in grey. **d**, Heatmap showing expression (log2(intensity)) of DE phosphosites (PS) enriched upon IR treatment. **e**, Top 25 GO biological processes enriched in samples exposed to IR; *P* value, hypergeometric test, Bonferroni corrected. **f**, Distribution of amino acid residues surrounding the DE phosphosites enriched in irradiated (upper panel) or not irradiated (lower panel) samples as determined by IceLogo software. See also Supplementary Fig. 3.

resistance factors, with 24 candidates, including 53BP1, identified by all three approaches (**Fig. 4c**, **Supplementary Table 2** and **Table 1**). Furthermore, we found loss of REV7, HELB and PARG to be associated with PARPi resistance, consistent with our previous *in vitro* and *in vivo* studies involving KB1P(M) and KB2P models[17,30,44]. Downstream of 53BP1, we also identified frameshift mutations (predicted loss-of-function) in the *Rif1* gene in 3 PARPi-

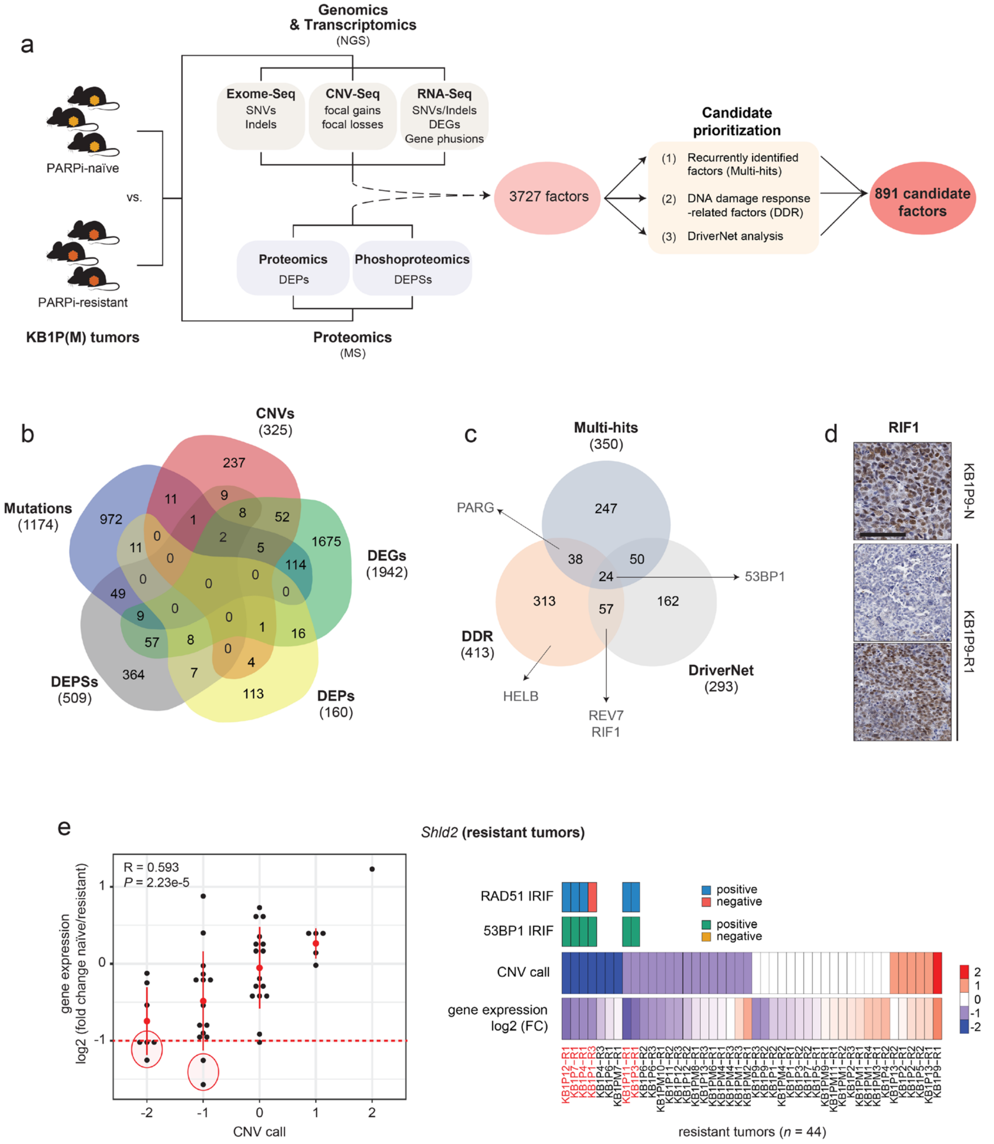

resistant tumors. Subsequent IHC analysis revealed that RIF1 expression was completely lost in a large area (~50%) of the KB1P9-R1 resistant tumor (all naïve tumors were RIF1 positive) (**Fig. 4d**). This pattern did not correlate with the *Rif1* mutational status, however, most likely due to the intratumor heterogeneity. Loss of RIF1 in the KB1P9-R1 tumor matched with the detected RAD51 IRIF restoration in the presence of 53BP1 foci (**Fig. 2a**), which is in agreement with the role of RIF1 in the 53BP1 pathway. At the time of our analysis three components of the shieldin complex, SHLD1, SHLD2 and SHLD3, were not annotated as factors involved in the DDR. We therefore examined their potential contribution to PARPi resistance in a retrospective fashion. As shown in **Fig. 4e**, decreased expression and concomitant copy number loss of the *Shld2* locus were found in 6 out of 44 resistant KB1P(M) cases. Moreover, aberrations in *Shld2* were mutually exclusive with the loss of 53BP1 and in 5/6 cases matched with the HR recovery. Hence, of the recently identified new shieldin complex members, we find loss of *Shld2* back as mechanism of secondary PARPi resistance in our mouse model for *BRCA1*-mutated breast cancer.

DISCUSSION

In our study we used PARPi-resistance as a tool to probe for different activities of BRCA1 and BRCA2 in DNA repair. Our analysis of emerged drug resistance mechanisms confirmed a clear functional distinction between these two factors.

BRCA1 and BRCA2 are often mentioned together, partly owing to their tumor suppressor activities and roles in homology-directed repair. From a biological standpoint, however, BRCA1 and BRCA2 are not functionally redundant in HR. The epistatic relationship between BRCA1 and BRCA2 was first put forward in the context of embryonic lethality by Ludwig *et al* almost 20 years ago[45]. Consistent with this relationship, previous work from our laboratory

---

◀ **Figure 4.** Multi-omics analysis of KB1P(M) tumors identifies putative factors involved in PARP inhibitor resistance. **a**, Schematic of integrative multi-omics analysis of matched PARPi-naïve and resistant KB1P(M) tumors. SNVs – single nucleotide variants, DEGs – differentially expressed (DE) genes, DEPs – DE proteins, DEPSs – DE phosphosites; NGS – next-generation sequencing, MS – mass spectrometry. **b**, Venn diagram showing the overlap between the different analyses (initial 3727 candidates, before the prioritization); numbers in the brackets indicate the total number of events identified in a given dataset. **c**, Venn diagram showing the overlap between the different prioritization methods (final 891 factors); number in the brackets indicate the total number of factors yielded by an indicated method; known PARPi-resistance factors are highlighted. **d**, RIF1 IHC staining of KB1P9 PARPi-naïve and-resistant tumors (-N and-R1, respectively); scale bar, 100 µm. **e**, Gene expression (RNA-Seq) and copy number variation data for *Shld2* across KB1P(M) PARPi-resistant tumors; left panel - correlation between *Shld2* gene expression and copy-number estimation for a panel of KB1P(M) tumors (single data points represent individual tumors; R (coefficient) and *P* value of Spearman correlation are shown; red dot and error bars - mean expression value ± SD), right panel – oncoplot showing RAD51 and 53BP1 IRIF status of tumors with >50% decrease in *Shld2* expression and loss of *Shld2* gene copy (samples indicated in red; see also Fig. 2a).

Table 1 List of the top 24 PARPi-resistance candidate factors identified by integrative multi-omics analysis of KB1P(M) tumors. DE – differentially expressed; no gene fusions were found for the indicated factors.

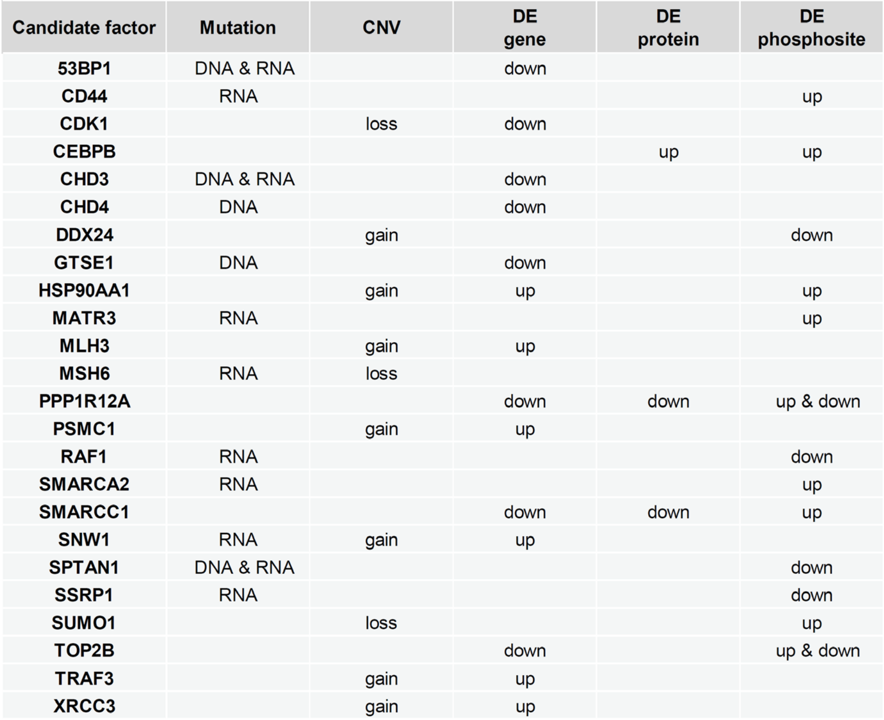

Candidate factor	Mutation	CNV	DE gene	DE protein	DE phosphosite
53BP1	DNA & RNA		down		
CD44	RNA				up
CDK1		loss	down		
CEBPB				up	up
CHD3	DNA & RNA		down		
CHD4	DNA		down		
DDX24		gain			down
GTSE1	DNA		down		
HSP90AA1		gain	up		up
MATR3	RNA				up
MLH3		gain	up		
MSH6	RNA	loss			
PPP1R12A			down	down	up & down
PSMC1		gain	up		
RAF1	RNA				down
SMARCA2	RNA				up
SMARCC1			down	down	up
SNW1	RNA	gain	up		
SPTAN1	DNA & RNA				down
SSRP1	RNA				down
SUMO1		loss			up
TOP2B			down		up & down
TRAF3		gain	up		
XRCC3		gain	up		

demonstrated that concomitant tissue-specific deletion of the *Brca1* and *Brca2* genes (KB1B2P) resulted in similar tumor development as single gene knockouts (KB1P and KB2P) (Holstege, Liu, Jonkers et al., unpublished data). Here, we show that functional differences between BRCA1 and BRCA2 also impact the resistance patterns in PARPi-treated tumors. While the HR-deficient phenotype of *Brca1* null cells could be largely suppressed by PARPi-induced inactivation of the 53BP1-RIF1-shieldin pathway, tumors with *Brca2* deletion completely failed to rescue HR activity. These results underline the essential role of BRCA2 in RAD51 loading during the HR process. Interestingly, in contrast to HR, BRCA2 seems dispensable for the RAD51-mediated fork reversal and protection of stalled RF, as shown by previous studies[26,46].

Clinical utility of RAD51 nuclear foci as a surrogate marker of HR activity has been recently evaluated in the context of PARPi response[47]. Our results point to an important limitation of this method, as we show that PARPi resistance can be triggered independently of HR, in both BRCA1- and BRCA2-deficient cancers. Ideally, additional functional and genetic tests should be carried out to confirm PARPi sensitivity in tumors with a negative RAD51 score. This should be enabled in near future by recent advances in tumor-derived organoid technology[48], use of liquid biopsies[8] and development of predictive mutational signatures[49] and may be informed by the identification of novel resistant factors. Our KB2P model provides a unique system to probe into HR-independent resistance, and we have recently reported that loss of PARG drives PARPi resistance regardless of the BRCA status[17]. This finding is corroborated using our multi-omics analysis in the KB1P(M) models which also yielded PARG as one of the putative resistance factors.

Our systematic analysis of RAD51 IRIF revealed that nearly 2/3 of the resistant KB1P(M) tumors restored functional HR in response to PARPi treatment. Despite the intratumor heterogeneity observed in our model, we obtained a good correlation between loss of 53BP1 and HR rescue. Moreover, by combining functional analyses with high-throughput omics data we were able to identify aberrations in downstream interactors and effectors of 53BP1, in particular RIF1, REV7 and SHLD2. Also here, the majority of the cases were RAD51 IRIF proficient and the alterations of these genes were largely mutually exclusive. Importantly, the levels of the RAD51 IRIF formation in the resistant tumors with positive RAD51 score were significantly lower than in BRCA-proficient controls (**Fig. 2c**), indicating sub-optimal levels of HR activity in these samples. A recent study by Nacson *et al*. suggested that BRCA1 is dispensable for the end resection, but not entirely redundant in the later step of the HR where it interacts with PALB2 and promotes RAD51 loading[50]. Thus, it is possible that in our model loss of 53BP1 rescues the resection defect but lack of BRCA1 activity downstream of resection limits the overall efficiency of repair. Nevertheless, we have shown before that 53BP1 depletion completely abolishes PARPi sensitivity of KB1P(M) tumors[23], suggesting that partial HR restoration is sufficient to suppress PARPi toxicity *in vivo*. Moreover, to best of our knowledge, it is not yet clear if loss of 53BP1 is sufficient to rescue the viability of *Brca1*-null embryos. 53BP1 deletion suppressed the embryonic lethality of mice with homozygous *Brca1* hypomorphic mutations (*Brca1*$^{\Delta 11/\Delta 11}$; *Brca1*$^{\Delta 2/\Delta 2}$), however did not suppress all of the phenotypes associated with *Brca1* loss, such as propensity to develop tumors or hypersensitivity to DNA damaging agents[50–53]. These results are in line with our findings and suggest that some of the DNA repair activities of BRCA1 cannot be alleviated by 53BP1 loss.

Our multi-omics approach for integrative data analysis yielded an extensive list of PARPi resistance candidates, which require further verification. Among the most prominent hits, we found inactivation of 53BP1 which attest to the validity of our approach. Intriguingly, we also found downregulation of CDK1 to be associated with PARPi resistance (**Table 1**). This is somehow unexpected, as compromised activity of CDK1 was previously shown to confer PARPi sensitivity of HR-proficient tumors[54]. Moreover, CDK1 was shown to be involved in restricting DSB repair during mitosis, to prevent 53BP1-dependent telomere fusion and aneuploidy[55]. Interestingly, KB1P(M) tumors with the strongest evidence of CDK1 loss had retained functional 53BP1 (data not shown). It would therefore be interesting to test the effect of CDK1 downregulation specifically in the BRCA1-deficient context.

As a next validation step, we plan to perform CRISPR-Cas9 functional genetic screens using a focused gRNA library targeting identified genes. This approach should be complemented by gain-of-function screens, as many of the factors were upregulated in resistant samples. Moreover, we have also generated a phosphoproteomic dataset, which could be used to identify biomarkers of PARPi resistance, which are not necessarily directly driving the resistant phenotype. Analysis of phosphorylation networks might reveal activation of alternative signaling pathways in tumors with defective HR. This would require more detailed analysis, however, and is beyond the scope of the current study.

Finally, although we show that resistance occurs and is influenced by the specific genetic context, it is important to stress that there are other factors that will contribute to the resistant patterns in the clinic. For example, PARP inhibitors that are very efficient in PARP trapping are more likely to induce mutations in *PARP1* than less potent PARP poisons. Future studies should address these aspects in more detail, and expanding use of PARPi in the clinic should soon provide clinical specimens that will allow us to verify the relevance of different PARPi mechanisms identified in our mouse models for BRCA1/2-deficient breast cancer.

ACKNOWLEDGEMENTS

We thank the members of the Preclinical Intervention Unit of the Mouse Clinic for Cancer and Ageing (MCCA) at the NKI for their technical support with the animal studies, and NKI core facilities: Animal Pathology facility, Digital Microscopy facility, Genomics Core facility and Animal facility for their excellent service. We would also like to acknowledge Marco Barazas for his help in setting up the RIF1 IHC. Financial support came from the Dutch Cancer Society (KWF 2011-5220 and 2014-6532), the Netherlands Organization for Scientific Research (VICI 91814643 and a National Roadmap grant for Large-Scale Research Facilities), the Netherlands Genomics Initiative (93512009), the Swiss National Science Foundation (310030_156869), the Swiss Cancer League (KLS-4282-08-2017) and the European Research Council (CoG-681572 to S.R., SyG-319661 to J.J.).

AUTHOR CONTRIBUTIONS

Conceptualization, E.G., S.R., J.J.; Methodology, E.G., F.R., J.B., S.R.P.; Investigation, E.G., F.R., J.B., A.A.D., W.S.; Software and Formal Analysis, E.G., F.R., J.B., B.v.d.B., J.R.d.R., R.d.B.; Writing – Original Draft, Review & Editing – E.G., P.B., J.J., S.R.; Supervision, M.v.d.V., C.R.J., L.F.A.W., P.B., J.J., S.R.; Funding Acquisition, J.J. and S.R.

REFERENCES

1. Groenendijk, F. H. & Bernards, R. Drug resistance to targeted therapies: déjà vu all over again. *Mol Oncol* **8**, 1067–1083 (2014).
2. Braga, S. Resistance to Targeted Therapies in Breast Cancer. *Methods Mol. Biol.* **1395**, 105–136 (2016).
3. Farmer, H. *et al.* Targeting the DNA repair defect in BRCA mutant cells as a therapeutic strategy. *Nature* **434**, 917–921 (2005).
4. Bryant, H. E. *et al.* Specific killing of BRCA2-deficient tumours with inhibitors of poly(ADP-ribose) polymerase. *Nature* **434**, 913–917 (2005).
5. Ray Chaudhuri, A. & Nussenzweig, A. The multifaceted roles of PARP1 in DNA repair and chromatin remodelling. *Nat. Rev. Mol. Cell Biol.* **18**, 610–621 (2017).
6. Murai, J. *et al.* Trapping of PARP1 and PARP2 by Clinical PARP Inhibitors. *Cancer Res* **72**, 5588–5599 (2012).
7. Murai, J. *et al.* Differential trapping of PARP1 and PARP2 by clinical PARP inhibitors. *Cancer Res* **72**, 5588–5599 (2012).
8. Gogola, E., Rottenberg, S. & Jonkers, J. Resistance to PARP Inhibitors: Lessons from Preclinical Models of BRCA-Associated Cancer. **3**, (2019).
9. Schoonen, P. M. *et al.* Progression through mitosis promotes PARP inhibitor-induced cytotoxicity in homologous recombination-deficient cancer cells. *Nat Commun* **8**, 15981 (2017).
10. Mateo, J. *et al.* DNA-Repair Defects and Olaparib in Metastatic Prostate Cancer. *N. Engl. J. Med.* **373**, 1697–1708 (2015).
11. Waddell, N. *et al.* Whole genomes redefine the mutational landscape of pancreatic cancer. *Nature* **518**, 495–501 (2015).
12. Nik-Zainal, S. *et al.* Landscape of somatic mutations in 560 breast cancer whole-genome sequences. *Nature* **534**, 47–54 (2016).
13. Patch, A.-M. *et al.* Whole-genome characterization of chemoresistant ovarian cancer. *Nature* **521**, 489–494 (2015).
14. Homologous Recombination Deficiency in Breast Cancer: A Clinical Review | JCO Precision Oncology. Available at: http://ascopubs.org/doi/abs/10.1200/PO.16.00031. (Accessed: 9th December 2018)
15. Lord, C. J. & Ashworth, A. PARP inhibitors: Synthetic lethality in the clinic. *Science* **355**, 1152–1158 (2017).
16. Rottenberg, S. *et al.* Selective induction of chemotherapy resistance of mammary tumors in a conditional mouse model for hereditary breast cancer. *Proc. Natl. Acad. Sci. U.S.A.* **104**, 12117–12122 (2007).
17. Gogola, E. *et al.* Selective Loss of PARG Restores PARylation and Counteracts PARP Inhibitor-Mediated Synthetic Lethality. *Cancer Cell* **33**, 1078-1093.e12 (2018).
18. Murai, J. *et al.* SLFN11 Blocks Stressed Replication Forks Independently of ATR. *Mol. Cell* **69**, 371-384.e6 (2018).
19. Murai, J. *et al.* Resistance to PARP inhibitors by SLFN11 inactivation can be overcome by ATR inhibition. *Oncotarget* **7**, 76534–76550 (2016).
20. Cantor, S. B. & Calvo, J. A. Fork Protection and Therapy Resistance in Hereditary Breast Cancer. *Cold Spring Harb. Symp. Quant. Biol.* (2018). doi:10.1101/sqb.2017.82.034413
21. Weigelt, B. *et al.* DiverseBRCA1andBRCA2Reversion Mutations in Circulating Cell-Free DNA of Therapy-Resistant Breast or Ovarian Cancer. *Clin. Cancer Res.* **23**, 6708–6720 (2017).
22. Ang, J. E. *et al.* Efficacy of chemotherapy in BRCA1/2 mutation carrier ovarian cancer in the setting of PARP inhibitor resistance: a multi-institutional study. *Clin. Cancer Res.* **19**, 5485–5493 (2013).

23. Jaspers, J. E. *et al.* Loss of 53BP1 causes PARP inhibitor resistance in Brca1-mutated mouse mammary tumors. *Cancer Discov* **3**, 68–81 (2013).

24. Jonkers, J. *et al.* Synergistic tumor suppressor activity of BRCA2 and p53 in a conditional mouse model for breast cancer. *Nat. Genet.* **29**, 418–425 (2001).

25. Liu, X. *et al.* Somatic loss of BRCA1 and p53 in mice induces mammary tumors with features of human BRCA1-mutated basal-like breast cancer. *Proc. Natl. Acad. Sci. U.S.A.* **104**, 12111–12116 (2007).

26. Ray Chaudhuri, A. *et al.* Replication fork stability confers chemoresistance in BRCA-deficient cells. *Nature* **535**, 382–387 (2016).

27. Oplustil O'Connor, L. *et al.* The PARP Inhibitor AZD2461 Provides Insights into the Role of PARP3 Inhibition for Both Synthetic Lethality and Tolerability with Chemotherapy in Preclinical Models. *Cancer Res.* **76**, 6084–6094 (2016).

28. Godin, S. K., Sullivan, M. R. & Bernstein, K. A. Novel insights into RAD51 activity and regulation during homologous recombination and DNA replication. *Biochem. Cell Biol.* **94**, 407–418 (2016).

29. Rottenberg, S. *et al.* High sensitivity of BRCA1-deficient mammary tumors to the PARP inhibitor AZD2281 alone and in combination with platinum drugs. *Proc. Natl. Acad. Sci. U.S.A.* **105**, 17079–17084 (2008).

30. Xu, G. *et al.* REV7 counteracts DNA double-strand break resection and affects PARP inhibition. *Nature* **521**, 541–544 (2015).

31. Dev, H. *et al.* Shieldin complex promotes DNA end-joining and counters homologous recombination in BRCA1-null cells. *Nat. Cell Biol.* **20**, 954–965 (2018).

32. Gupta, R. *et al.* DNA Repair Network Analysis Reveals Shieldin as a Key Regulator of NHEJ and PARP Inhibitor Sensitivity. *Cell* **173**, 972-988.e23 (2018).

33. Ghezraoui, H. *et al.* 53BP1 cooperation with the REV7-shieldin complex underpins DNA structure-specific NHEJ. *Nature* **560**, 122–127 (2018).

34. Noordermeer, S. M. *et al.* The shieldin complex mediates 53BP1-dependent DNA repair. *Nature* **560**, 117–121 (2018).

35. Linding, R. *et al.* Systematic discovery of in vivo phosphorylation networks. *Cell* **129**, 1415–1426 (2007).

36. Hornbeck, P. V. *et al.* PhosphoSitePlus, 2014: mutations, PTMs and recalibrations. *Nucleic Acids Res.* **43**, D512-520 (2015).

37. Bennetzen, M. V. *et al.* Site-specific phosphorylation dynamics of the nuclear proteome during the DNA damage response. *Mol. Cell Proteomics* **9**, 1314–1323 (2010).

38. Bensimon, A. *et al.* ATM-dependent and-independent dynamics of the nuclear phosphoproteome after DNA damage. *Sci Signal* **3**, rs3 (2010).

39. Zhou, C. *et al.* Profiling DNA damage-induced phosphorylation in budding yeast reveals diverse signaling networks. *Proc Natl Acad Sci U S A* **113**, E3667–E3675 (2016).

40. Bensimon, A., Aebersold, R. & Shiloh, Y. Beyond ATM: the protein kinase landscape of the DNA damage response. *FEBS Lett.* **585**, 1625–1639 (2011).

41. Yeh, Y.-H., Huang, Y.-F., Lin, T.-Y. & Shieh, S.-Y. The cell cycle checkpoint kinase CHK2 mediates DNA damage-induced stabilization of TTK/hMps1. *Oncogene* **28**, 1366–1378 (2009).

42. Wei, J.-H. *et al.* TTK/hMps1 participates in the regulation of DNA damage checkpoint response by phosphorylating CHK2 on threonine 68. *J. Biol. Chem.* **280**, 7748–7757 (2005).

43. Bashashati, A. *et al.* DriverNet: uncovering the impact of somatic driver mutations on transcriptional networks in cancer. *Genome Biol.* **13**, R124 (2012).

44. Tkáč, J. *et al.* HELB Is a Feedback Inhibitor of DNA End Resection. *Mol. Cell* **61**, 405–418 (2016).

45. Ludwig, T., Chapman, D. L., Papaioannou, V. E. & Efstratiadis, A. Targeted mutations of breast cancer susceptibility gene homologs in mice: lethal phenotypes of Brca1, Brca2, Brca1/Brca2, Brca1/p53, and Brca2/p53 nullizygous embryos. *Genes Dev.* **11**, 1226–1241 (1997).

46. Mijic, S. *et al.* Replication fork reversal triggers fork degradation in BRCA2-defective cells. *Nat Commun* **8**, (2017).

47. Castroviejo-Bermejo, M. *et al.* A RAD51 assay feasible in routine tumor samples calls PARP inhibitor response beyond BRCA mutation. *EMBO Mol Med* **10**, (2018).

48. Xu, H. *et al.* Organoid technology and applications in cancer research. *J Hematol Oncol* **11**, (2018).

49. Davies, H. *et al.* HRDetect is a predictor of BRCA1 and BRCA2 deficiency based on mutational signatures. *Nat. Med.* **23**, 517–525 (2017).

50. Nacson, J. *et al.* BRCA1 Mutation-Specific Responses to 53BP1 Loss-Induced Homologous Recombination and PARP Inhibitor Resistance. *Cell Rep* **24**, 3513-3527.e7 (2018).

51. Bunting, S. F. *et al.* 53BP1 inhibits homologous recombination in Brca1-deficient cells by blocking resection of DNA breaks. *Cell* **141**, 243–254 (2010).

52. Cao, L. *et al.* A selective requirement for 53BP1 in the biological response to genomic instability induced by Brca1 deficiency. *Mol. Cell* **35**, 534–541 (2009).

53. Li, M. *et al.* 53BP1 ablation rescues genomic instability in mice expressing 'RING-less' BRCA1. *EMBO Rep.* **17**, 1532–1541 (2016).

54. Johnson, N. *et al.* Compromised CDK1 activity sensitizes BRCA-proficient cancers to PARP inhibition. *Nat. Med.* **17**, 875–882 (2011).

55. Orthwein, A. *et al.* Mitosis inhibits DNA double-strand break repair to guard against telomere fusions. *Science* **344**, 189–193 (2014).

56. Martin, M. Cutadapt removes adapter sequences from high-throughput sequencing reads. *EMBnet. journal* **17**, 10–12 (2011).

57. Dobin, A. *et al.* STAR: ultrafast universal RNA-seq aligner. *Bioinformatics* **29**, 15–21 (2013).

58. Garrison, E. & Marth, G. Haplotype-based variant detection from short-read sequencing. *arXiv:1207.3907 [q-bio]* (2012).

59. Cingolani, P. *et al.* A program for annotating and predicting the effects of single nucleotide polymorphisms, SnpEff: SNPs in the genome of Drosophila melanogaster strain w1118; iso-2; iso-3. *Fly (Austin)* **6**, 80–92 (2012).

60. Liao, Y., Smyth, G. K. & Shi, W. featureCounts: an efficient general purpose program for assigning sequence reads to genomic features. *Bioinformatics* **30**, 923–930 (2014).

61. Robinson, M. D., McCarthy, D. J. & Smyth, G. K. edgeR: a Bioconductor package for differential expression analysis of digital gene expression data. *Bioinformatics* **26**, 139–140 (2010).

62. Law, C. W., Chen, Y., Shi, W. & Smyth, G. K. voom: Precision weights unlock linear model analysis tools for RNA-seq read counts. *Genome Biol.* **15**, R29 (2014).

63. Ronde, J. J. de, Rigaill, G., Rottenberg, S., Rodenhuis, S. & Wessels, L. F. A. Identifying subgroup markers in heterogeneous populations. *Nucleic Acids Research* **41**, e200 (2013).

64. Haas, B. *et al.* STAR-Fusion: Fast and Accurate Fusion Transcript Detection from RNA-Seq. *bioRxiv* 120295 (2017). doi:10.1101/120295

65. Li, H. Aligning sequence reads, clone sequences and assembly contigs with BWA-MEM. *arXiv:1303.3997 [q-bio]* (2013).

66. Scheinin, I. *et al.* DNA copy number analysis of fresh and formalin-fixed specimens by shallow whole-genome sequencing with identification and exclusion of problematic regions in the genome assembly. *Genome Res.* **24**, 2022–2032 (2014).

67. van Dyk, E., Hoogstraat, M., ten Hoeve, J., Reinders, M. J. T. & Wessels, L. F. A. RUBIC identifies driver genes by detecting recurrent DNA copy number breaks. *Nat Commun* **7**, (2016).

68. Piersma, S. R. *et al.* Feasibility of label-free phosphoproteomics and application to base-line signaling of colorectal cancer cell lines. *J Proteomics* **127**, 247–258 (2015).

69. Tyanova, S., Temu, T. & Cox, J. The MaxQuant computational platform for mass spectrometry-based shotgun proteomics. *Nat Protoc* **11**, 2301–2319 (2016).
70. Cox, J. & Mann, M. MaxQuant enables high peptide identification rates, individualized p.p.b.-range mass accuracies and proteome-wide protein quantification. *Nat. Biotechnol.* **26**, 1367–1372 (2008).
71. Ritchie, M. E. *et al.* limma powers differential expression analyses for RNA-sequencing and microarray studies. *Nucleic Acids Res.* **43**, e47 (2015).
72. Cox, J. *et al.* Accurate proteome-wide label-free quantification by delayed normalization and maximal peptide ratio extraction, termed MaxLFQ. *Mol. Cell Proteomics* **13**, 2513–2526 (2014).
73. Bindea, G. *et al.* ClueGO: a Cytoscape plug-in to decipher functionally grouped gene ontology and pathway annotation networks. *Bioinformatics* **25**, 1091–1093 (2009).
74. Shannon, P. *et al.* Cytoscape: a software environment for integrated models of biomolecular interaction networks. *Genome Res.* **13**, 2498–2504 (2003).
75. Colaert, N., Helsens, K., Martens, L., Vandekerckhove, J. & Gevaert, K. Improved visualization of protein consensus sequences by iceLogo. *Nat. Methods* **6**, 786–787 (2009).
76. Andrés-León, E., Cases, I., Arcas, A. & Rojas, A. M. DDRprot: a database of DNA damage response-related proteins. *Database (Oxford)* **2016**, (2016).
77. Horn, H. *et al.* KinomeXplorer: an integrated platform for kinome biology studies. *Nat. Methods* **11**, 603–604 (2014).
78. Miller, M. L. *et al.* Linear motif atlas for phosphorylation-dependent signaling. *Sci Signal* **1**, ra2 (2008).

METHODS

In situ RAD51/53BP1 IRIF formation assay

All animal experiments were approved by the Animal Ethics Committee of The Netherlands Cancer Institute (Amsterdam, the Netherlands) and performed in accordance with the Dutch Act on Animal Experimentation (November 2014). Cryopreserved material of PARPi-naïve or -resistant KB1P, KB1PM and KB2P tumors (KB1P(M): 23 naïve, 47 resistant; KB2P: 19 naïve, 26 resistant) was thawed and orthotopically engrafted into the right mammary fat pad of 6 week-old wild-type female mice (KB1P(M) – FVB; KB2P – FVB:129/Ola(F1)). Tumor volume was monitored starting from two weeks after transplantations and calculated using the following formula: 0.5 x length x width^2. When tumors reached approximately 500 mm^3 (100% relative tumor volume), they were locally irradiated (dose 15 Gy, unless otherwise stated) using a CT-guided high precision cone beam micro-irradiator (X-RAD 225Cx) or left untreated (control). Two hours post irradiation tumors were isolated and part of the tissue was immediately fixed in 4% (w/v) solution of formaldehyde in PBS (remaining tissue was fresh frozen for the proteomic and phosphoproteomic analyses). 5 µm-thick FFPE (formalin-fixed paraffin embedded) tissue sections were then used for immunofluorescence. Following deparaffinization (70°C, 20 min), tissues were rehydrated and cooked in DAKO Target Retrieval Solution pH 9 (#S236784, DAKO) for 20 min in microwave at ~600W, to allow antigen retrieval. Next, tissue permeabilization was achieved by incubating samples in 0.2% (v/v) Triton X-100 in PBS for 20 min and followed by 1 hr DNAse (1,000 U/ml; #04536282001, Roche) treatment at 37°C. Blocking was done for 30 min in staining buffer (1% (w/v) BSA, 0.15% (w/v) glycine and 0.1% (v/v) Triton X-100 in PBS). Subsequent incubation with primary antibodies was carried out overnight at 4°C, and later with secondary antibodies for 1 hr at room temperature. The following antibodies (diluted in staining buffer) were used in this assay: rabbit polyclonal anti-RAD51 (kind gift from R. Kanaar, Erasmus MC, Rotterdam; 1:5,000), rabbit polyclonal anti-53BP1 (#ab21083, Abcam; 1:1,000), goat polyclonal anti-rabbit, Alexa Fluor® 658-conjugated (#A11011, Thermo Fisher Scientific; diluted 1:1,000). Samples were mounted with VECTASHIELD Hard Set Mounting Media with DAPI (#H-1500; Vector Laboratories). Images were taken with Leica SP5 (Leica Microsystems) confocal system equipped with a x100 objective and image stacks (~6 slices) were analyzed using an in-house developed ImageJ macro to automatically and objectively quantify IR-induced foci, as described before[30]. Briefly, nuclei were segmented by thresholding the (median-filtered) DAPI signal, followed by a watershed operation to separate touching nuclei. For each *z*-stack the maximum-intensity projection of the foci signal was background-subtracted using a difference of gaussians method. Next, for every nucleus, foci candidates were identified as locations where the resulting pixel values exceeded the background by a factor (typically 25x) times the median standard deviation of all nuclei in the image. Additional filters for discriminating for foci size, nucleus size (to eliminate stromal cells) and absolute brightness were applied. Results were validated by visual inspection. Visualization as well as quantification of foci was done in a blinded fashion. For each sample, five random areas (246 x 246 µm; on average 125 cells per area) were imaged and analyzed. Cell was considered positive if contained >5 nuclear foci. KP tumor was used as a positive control in this assay.

53BP1 and RIF1 immunohistochemistry (IHC)

All IHC stainings were performed on FFPE material. For 53BP1 IHC, tissue sections were boiled for 30 min in citrate buffer pH 6.0 (#CBB 999, Scytek Laboratories) to facilitate antigen retrieval. Next, the stainings were carried out by using 3% (v/v) H_2O_2 solution in methanol for blocking endogenous peroxidase activity (20 min) and 4% BSA plus 5% normal goat serum (NGS) in PBS as a blocking buffer (30 min). Primary antibodies were diluted in 1.25% NGS plus 1% BSA in PBS, and applied on the samples overnight, at 4°C. Incubation with secondary antibodies (diluted in 1.25% NGS/1% BSA in PBS; 30 min, room temperature) (#E0433, DakoCytomation) was followed by incubation with streptavidin conjugated to horseradish peroxidase (1:200; 1.25% NGS/1% BSA in PBS; 30 min) (#P0397, DakoCytomation). For visualization DAB (#D5905, Sigma), H_2O_2 (#A-31642, Sigma, 1:1,250) and hematoxylin counterstaining were applied. IHC stainings were evaluated and scored (0 – negative, 1 – low expression, 2 – high expression) by a pathologist who was blinded regarding the identity of the samples. RIF1 IHC was performed using the same protocol except antigen retrieval step was carried out for 20 min and normal donkey serum was used instead of NGS. Antibodies used in this protocol: goat polyclonal anti-RIF1 (E-20) (#sc-65191, Santa Cruz; 1:400), rabbit polyclonal anti-53BP1 (#A300-272A, Bethyl Laboratories; 1:1,000), secondary donkey-anti-goat-Bio (#E0433, DakoCytomation; 1:200), secondary goat-anti-rabbit-Bio (#E0432, Dako Cytomation; 1:1,000).

RNA and genomic DNA isolation

Genomic DNA was isolated from fresh frozen tumor tissue using a standard Proteinase K and phenol:chloroform extraction.

To isolate RNA, small pieces of fresh frozen tumor tissue were placed in 1 ml of TRIsure reagent (#BIO-38032, Bioline) and tissue lysis was achieved by high-speed shaking with stainless steel beads for 10 min, 50 Hz at room temperature (TissueLyser LT, Qiagen). Homogenized tissue lysates were further processed according to the TRIsure manufacturer’s protocol.

RNA Sequencing (RNA-Seq)

RNA-Seq data was generated as described before[17]. The resulting reads were trimmed using Cutadapt[56] and aligned to the GRCm35 reference genome using STAR (version 2.5.2b)[57]. First, to identify the SNVs and Indels, Freebayes variant caller was used with the mode of pooled-continuous (min-alternate-fraction = 0.1, min-alternate-count = 3)[58] and resulting variants were annotated by SnpEff[59]. We excluded the variants located in UTR regions or synonymous variants for downstream analysis. Next, to identify differentially expressed (DE) genes, gene expression counts were first generated by featureCounts using gene definitions from Ensembl GRCm38 (version 76)[60]. Genes with counts per million (CPM) larger than one in at least 10% of samples were used for further analysis. Trimmed mean of M-value (TMM) normalization was applied to the data using edgeR[61] and Limma-voom was used to correct for the donor effect and identify the differentially expressed genes (naïve vs resistant; FDR < 0.25)[62]. Because of the intratumoral heterogeneity, we additionally applied DIDS (Detection of Imbalanced Differential Signal) for the detection of subgroup markers in resistant populations ($p < 0.05$)[63]. The DE genes yielded by either Limma-voom or DIDS were used for multi-omics analysis. Finally, we applied STAR-fusion algorithm using fastq files after trimming process for the identification of gene fusions[64].

Whole-Exome Sequencing (WES)

For WES, genomic DNA was first sheared to approximately 300 bp fragments using Covaris S2 sonicator. Next, 500-1000 ng of sheared DNA was used as a template for a 6-cycle PCR to construct a fragmented library using the KAPA HTP Library Preparation Kit (Roche). Exome enrichment was performed using SeqCap EZ Enrichment Kit (Roche) according to the manufacturer's protocol (SeqCap EZ Library SR User's Guide, v5.3). Samples were sequenced on an Illumina HiSeq2500 (Illumina). Adapters in the resulting reads were trimmed using Cutadapt[56] (version 1.12) and the trimmed reads were aligned to the GRCm38 reference genome using BWA (version 0.7.15)[65]. The resulting alignments were sorted and marked for duplicates with Picard tools (version 2.5.0). Freebayes variant caller was used to identify SNVs and Indels for each sample with the mode of pooled-continuous (min-alternate-fraction = 0.1, min-alternate-count = 3, and min-coverage = 10)[58] and resulting variants were annotated by SnpEff[59]. We excluded the variants located in UTR regions or synonymous variants for downstream analysis.

Copy-Number Variation Sequencing (CNV-Seq)

CNV-Seq data was generated as described before[17]. Resulting reads were trimmed, sorted and marked for duplicates using the same pipeline as for the WES. The resulting alignments were analyzed to generate segmented profile differences between matched (naïve/resistant) samples derived from theh same tumor donor using the QDNAseq and QDNAseq.

mm10 packages (Bioconductor; bin size = 50K)[66]. To identify regions with recurrent copy number difference (naïve vs resistant), we iteratively ran RUBIC (focal threshold = 1e+08, min probes = 4, FDR < 0.25) with different cutoffs for calling amplifications and deletions (amp.level and del.level = 0.1, 0.2, 0.3, 0.4, 0.5) and selected genes within identified regions for all cutoffs for downstream analysis[67].

Preparation of tissue lysates and phosphopeptide enrichment

For the proteomic and phosphoproteomic analyses we used fresh frozen tissues from the BRCA1-deficient tumors generated for the RAD51 IRIF assay. To prepare the lysates, tumor tissues were first sliced into 10 µm-thick sections at-20°C. For each tumor, two distal sections were processed (replicates) and for each replicate around 10 mg of tissue was used, which resulted in a final amount of ~1 mg of protein per replicate. Sliced tissue was lysed in lysis buffer containing 9 M urea, 20 mM HEPES pH 8.0, 1 mM Na_3VO_4 (orthovanadate), 2.5 mM $Na_4P_2O_7$ (pyrophosphate) and 1nM $Na_2C_3H_7PO_6$ (β-glycerophosphate) at a tissue (mg) to buffer (µl) ratio of 1:20, vortexed and subsequently sonicated (3 cycles, 15 seconds on, 60 seconds off, maximum amplitude; Branson high intensity cuphorn sonicator). After lysis the protein concentration was determined using Pierce BCA Protein Assay Kit (#23225, Thermo Scientific). Next, lysate was reduced in 4 mM dithiothreitol (DTT; 20 min, 60°C), cooled to room temperature and alkylated in 10 mM iodoacetamide (15 min, in dark). Lysates were diluted to 2 M ure with 20 mM HEPES buffer pH 8.0 and digested with trypsin (10 µg/mg protein; overnight, 37°C). Digestion was terminated with 0.1% trifluoroacetic acid (TFA). Samples were stored at -80°C. Phosphopeptide enrichment using titanium dioxide (TioX) beads was carried out as described before[68]. For total proteome analysis, the non-bound fraction from the phosphopeptide enrichment was diluted to 0.1 µg/µl in loading solvent (4% ACN + 0.5% TFA in MilliQ water), and 1µg was injected on column.

LC-MS/MS

Peptides were separated by an Ultimate 3000 nanoLC-MS/MS system (Dionex LC-Packings, Amsterdam, The Netherlands) equipped with a 40 cm × 75 µm ID fused silica column custom packed with 1.9 µm 120 Å ReproSil Pur C18 aqua (Dr Maisch GMBH, Ammerbuch-Entringen, Germany). After injection, peptides were trapped at 6 µl/min on a 10 mm × 100 µm ID trap column packed with 5 µm 120 Å ReproSil Pur C18 aqua at 2% buffer B (buffer A: 0.5% acetic acid (Fischer Scientific), buffer B: 80% ACN, 0.5% acetic acid) and separated at 300 nl/min in a 10–40% buffer B gradient in 90 min (120 min inject-to-inject). The LC column was maintained at 50°C using a pencil-stype heater (Phoenix ST). Eluting peptides were ionized at a potential of +2 kVa into a Q Exactive mass spectrometer (Thermo Fisher, Bremen, Germany). Intact masses were measured at resolution 70.000 (at m/z 200) in the orbitrap using an AGC target value of 3 × 106 charges. The top 10 peptide signals (chargestates 2+ and higher) were submitted to MS/MS in the HCD (higher-energy collision) cell (1.6 amu isolation width, 25% normalized collision energy). MS/MS spectra were acquired at resolution 17.500 (at m/z 200) in the orbitrap using an AGC target value of 1 × 106 charges, a maxIT of 80 ms and an underfill ratio of 0.1% (resulting in an intensity threshold of 1.3 x104). Dynamic exclusion was applied with a repeat count of 1 and an exclusion time of 30 s.

Peptide and Protein identification

MS/MS spectra were searched against tmhe Uniprot Mus musculus reference_proteome (downloaded 2015_06 canonical and isoforms, 53216 entries) using MaxQuant 1.5.2.8[69,70]. Enzyme specificity was set to trypsin and up to two missed cleavages were allowed. Cysteine carboxamidomethylation (Cys, +57.021464 Da) was treated as fixed modification and serine, threonine and tyrosine phosphorylation (+79.966330 Da), methionine oxidation (Met,+15.994915 Da) and N-terminal acetylation (N-terminal, +42.010565 Da) as variable modifications. Peptide precursor ions were searched with a maximum mass deviation of 4.5 ppm and fragment ions with a maximum mass deviation of 20 ppm. Peptide, protein and site identifications were filtered at an FDR of 1% using the decoy database strategy. The minimal peptide length was 7 amino-acids and the minimum Andromeda score for modified peptides was 40 and the corresponding minimum delta score was 6 (default MaxQuant settings). Peptide identifications were propagated across samples with the match between runs option checked.

Label-free phosphopeptide quantification, global protein expression and data analysis

Phosphopeptides were quantified by their extracted ion intensities (‘Intensity’ in MaxQuant). MaxQuant output data (Phospho (STY)Sites.txt) was loaded into R 3.4.4 software environment for statistical computing and graphics and further processed using a custom script. In brief, decoy database hits, contaminants and non-class I phosphosites were excluded and the data matrix converted to account for the multiplicity of phosphorylations per peptide. Data were then log-transformed, normalized on the median intensity of all identified phosphosites and replicates averaged favoring data presence.

Limma package[71] was used to perform differential expression analysis. Furthermore, data were filtered for presence of at least 50% data points for the samples of each group (100% for small group sizes). In case of data presence in one group and absence in the second group, only observations with data points in at least 50% of the samples in one of these groups were manually included (100% for small group sizes).

Global protein expression analysis was based on MaxQuant LFQ Intensity[72]. Replicates were averaged, data was log-transformed and differential expression tested using the Limma package.

For gene ontology analysis of differentially regulated phosphosites, corresponding gene names were used as input for the ClueGo 2.5.1 extension[73] inside the Cytoscape 3.6.1 software[74] applying the standard settings and selecting biological process as repository for ontology. P value was computed using hypergeometric test and Bonferroni correction.

Phosphosite sequence logo analysis was performed using the iceLogo tool[75] and murine phosphosites listed in PhosphoSitePlus database (12.2017 release) were taken as reference set[36].

Pathway analysis of phosphosite candidates was performed using literature and DDRprot database[76].

For the prediction of upstream kinases, mouse phosphosites were mapped to their human orthologs using the PhosphoSitePlus database (12.2017 release)[36]. These orthologs were used as input for the NetworKIN tool[35,77,78] and resulting data further filtered, processed and visualized in R.

For discovery of phosphosites likely involved in PARPi resistance, first, naïve not irradiated samples were compared to their naïve irradiated counterparts as described above to prioritize for observations involved in DNA damage signaling. In a second step, naïve irradiated samples were compared to their resistant irradiated analogs. Phosphosites shared and differentially regulated in both of these two comparisons and showing either up- or downregulation in the resistant irradiated group were regarded as candidates possibly involved in PARPi resistance.

Statistical analysis

High-throughput genomics, transcriptomics, proteomics and phosphoproteomics data were analyzed as described in relevant Method sections. For the analysis of RAD51/53BP1 IRIF data we used two-tailed Mann-Whitney *U* test; **** $p < 0.0001$, *** $p < 0.001$, ** $p < 0.01$.

DATA AND SOFTWARE AVAILABILITY

Supplementary Table 1 and Supplementary Table 2: http://dx.doi.org/10.17632/ph3s6rztmv.1.

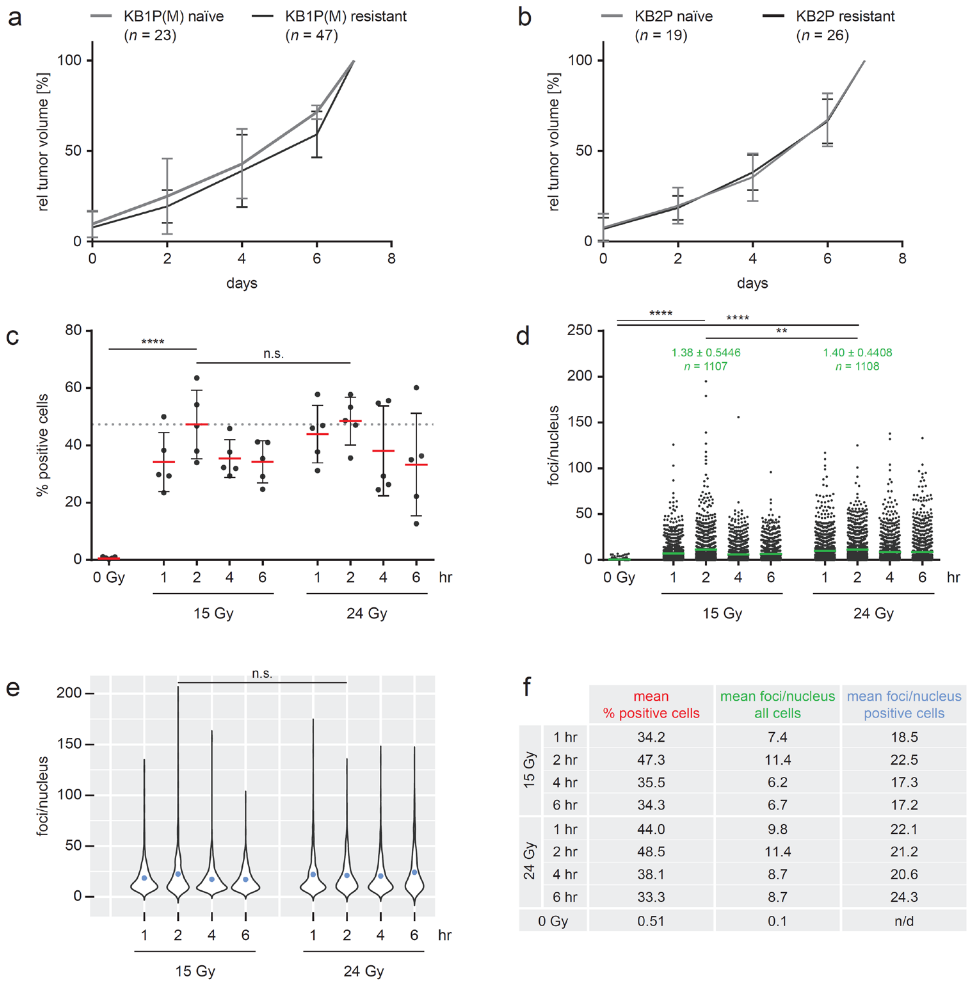

		mean % positive cells	mean foci/nucleus all cells	mean foci/nucleus positive cells
15 Gy	1 hr	34.2	7.4	18.5
	2 hr	47.3	11.4	22.5
	4 hr	35.5	6.2	17.3
	6 hr	34.3	6.7	17.2
24 Gy	1 hr	44.0	9.8	22.1
	2 hr	48.5	11.4	21.2
	4 hr	38.1	8.7	20.6
	6 hr	33.3	8.7	24.3
0 Gy		0.51	0.1	n/d

Supplementary Figure 1. Optimization of the RAD51 IRIF formation assay. **a, b** Growth curves of KB1P(M) (a) and KB2P (b) tumors, samples were irradiated at day 7. **c**, Percentage of RAD51 positive cells (>5 foci/nucleus) per tumor area (single data point) in a KP tumor irradiated with 0, 15 or 24 Gy, 1-6 hr post-irradiation; $****P < 0.0001$ (two-tailed Mann-Whitney *U* test); data shown as mean (red line) ± SD of a replicate, the experiment was repeated twice; grey dotted line indicates the mean value of a sample irradiated with 15 Gy and incubated for 2 hr. **d**, Number of foci per nucleus (single data point) quantified for the total tumor cell population of a KP described in (c); mean values are represented by green lines; $**P < 0.01$, statistical analysis as in (c). **e**, Number of foci per nucleus quantified for positive cell population (>5 foci/nucleus) of a KP tumor described in (c), and represented as violin plots showing the density (width = frequency) of the data; mean values are represented by blue dots; statistical analysis as in (c). **f**, Summary of analyses represented in (c-e).

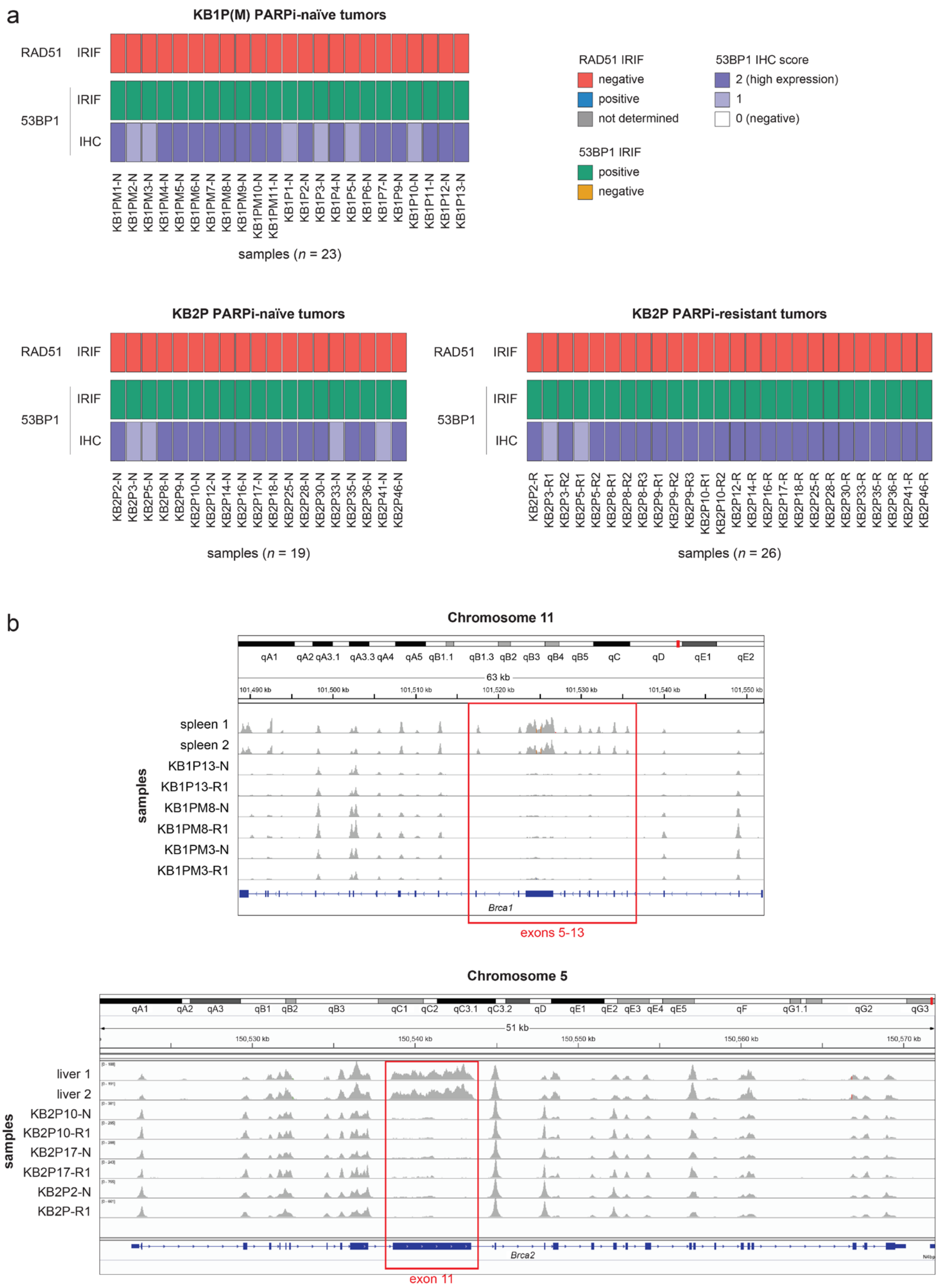

Supplementary Figure 2 Characterization of matched PARPi-naïve and-resistant KB1P(M) and KB2P tumors. **a**, Oncoplots summarizing the outcome of the indicated assays for KB1P PARPi-naïve and KB2P tumor panels. N – naïve, R – resistant. **b**, Visualization of exome sequencing reads for the *Brca1* and *Brca2* genes in KB1P(M) and KB2P tumor samples, respectively, and normal tissues (spleen1/2 and liver 1/2; controls), showing that deletions of specific exons (marked in red; *Brca1* – exons 5-13, *Brca2* – exon 11) are preserved in PARPi-naïve and-resistant tumor samples; data representative for the whole KB1P(M) and KB2P tumor panels.

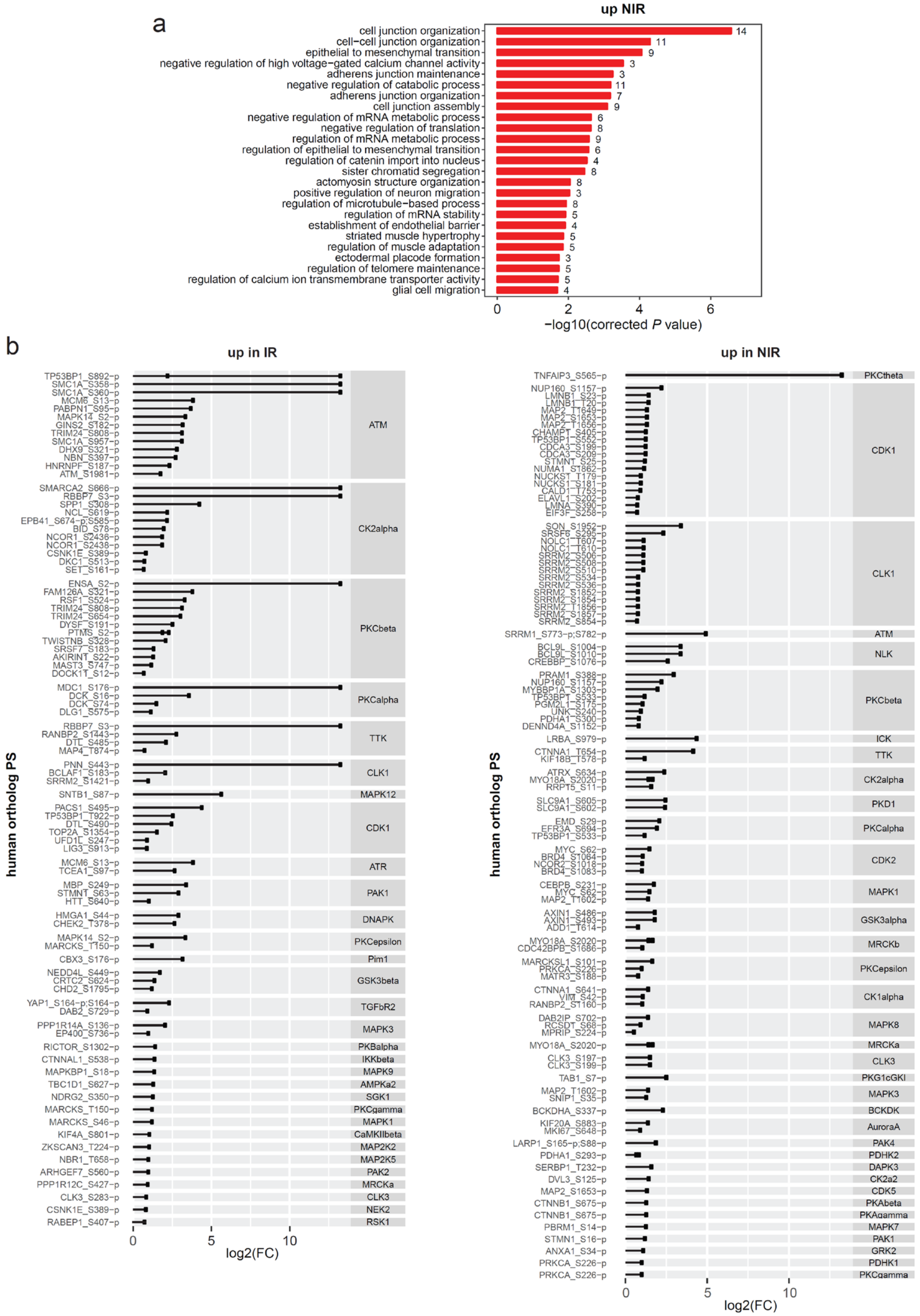

Supplementary Figure 3 IR-induced phosphorylation in KB1P(M) tumors. (**a**) Top 25 GO biological processes enriched in NIR samples; p value, hypergeometric test, Bonferroni corrected. (**b**) Kinase prediction analysis based on the PS enriched in IR (left panel) or NIR (right panel) samples; analysis performed with NetworKIN tool, using human ortholog PS; each bullet represents different phosphopeptide containing indicated PS.